

Focal Frequency Loss for Generative Models

Liming Jiang¹ Bo Dai¹ Wayne Wu² Chen Change Loy^{1✉}
¹S-Lab, Nanyang Technological University ²SenseTime Research
 {liming002, bo.dai, ccloy}@ntu.edu.sg wuwenyan@sensetime.com

Abstract

Despite the remarkable success of generative models in creating photorealistic images using deep neural networks, gaps could still exist between the real and generated images, especially in the frequency domain. In this study, we find that narrowing the frequency domain gap can ameliorate the image synthesis quality further. To this end, we propose the focal frequency loss, a novel objective function that brings optimization of generative models into the frequency domain. The proposed loss allows the model to dynamically focus on the frequency components that are hard to synthesize by down-weighting the easy frequencies. This objective function is complementary to existing spatial losses, offering great impedance against the loss of important frequency information due to the inherent crux of neural networks. We demonstrate the versatility and effectiveness of focal frequency loss to improve various baselines in both perceptual quality and quantitative performance.¹

1. Introduction

Generative models [17, 31, 12, 29, 56] have achieved remarkable performance in capturing high-dimensional representations of visual data and creating photorealistic images. Existing state-of-the-art generative models are mainly constructed using deep neural networks [27, 42, 43, 23]. Despite their immense success in image and video synthesis, one could still observe the gaps between the real and generated images in certain cases.

Sometimes these gaps are manifested in the form of artifacts that are discernible. For instance, upsampling layers using the transposed convolutions tend to produce checkerboard artifacts [41], an important cue that affects the perceptual quality of synthesized images. In other cases, the gaps may only be revealed through the frequency spectrum analysis. Recent studies [59, 74, 19] in media forensics have shown some notable periodic patterns in the frequency spectra of manipulated images, which may be consistent with artifacts in the spatial domain. In Figure 1, we show some

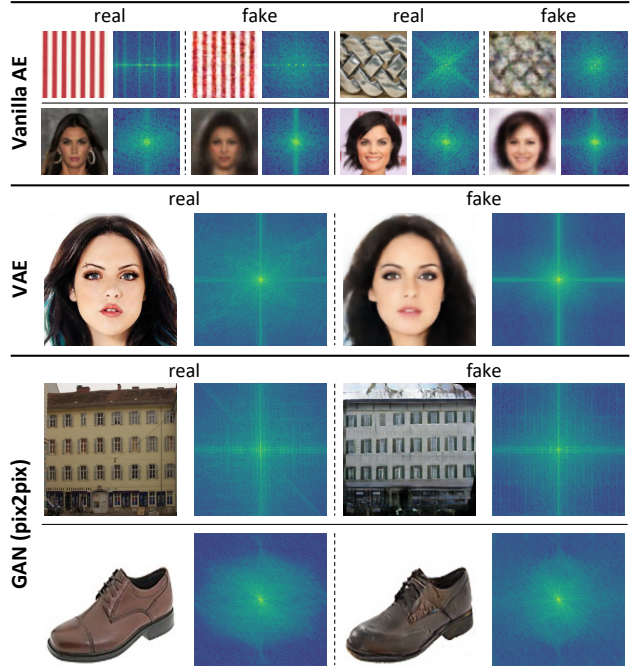


Figure 1. Frequency domain gaps between the real and the generated images by different types of generative models. Vanilla AE [17] loses important frequencies, leading to blurry images (Row 1 and 2). VAE [31] biases to a limited spectrum region (Row 3), losing high-frequency information (outer regions and corners). Unnatural periodic patterns can be spotted on the spectrum of images generated by GAN (pix2pix) [21] (Row 4), consistent with the observable checkerboard artifacts (zoom in for view). In some cases, a frequency spectrum region shift occurs to GAN-generated images (Row 5).

paired examples of real images and the fake ones synthesized by different generative models. It is observed that the frequency domain gap between the real and fake images may be a common issue for many generative models, albeit in slightly different forms.

The observed gaps between the real and fake images in the frequency domain may be imputed to some inherent crux of neural networks. Fourier analysis highlights a phenomenon called *spectral bias* [47, 38, 54], a learning bias of neural networks towards low-frequency functions. Thus,

¹GitHub: <https://github.com/EndlessSora/focal-frequency-loss>.

generative models tend to eschew hard frequencies and converge to an inferior point. *F-Principle* [68] shows that the priority of fitting certain frequencies in a network is also different throughout the training, usually from low to high. Consequently, it is difficult for a model to maintain important frequency information as it tends to generate frequencies with a higher priority.

In this paper, we study the frequency domain gap between real and fake images and explore ways to ameliorate synthesis quality by narrowing this gap. We aim at devising a generic loss function that is complementary to existing spatial losses. We set forth three yardsticks when designing this loss function: 1) The loss form is built on a space where frequencies of an image can be well represented and distinguished, facilitating optimization in the frequency dimension. 2) The loss enables a network to focus on frequency components that are hard to synthesize, *i.e.*, hard frequencies, which may be pivotal for further quality improvement. 3) The focused frequencies should be updated dynamically as the training proceeds to bridge the frequency domain gaps of different generative models adaptively.

To meet the aforementioned objectives, we carefully study the nature of frequency components in images. Existing methods [21, 42, 31] usually adopt pixel-level losses in the spatial domain, while spatial domain losses hardly help a network find the hard frequencies and synthesize them, in that every pixel shares the same significance. In comparison, we transform both the real and generated samples to their frequency representations using the standard discrete Fourier transform (DFT). The images are decomposed into sines and cosines, exhibiting the periodic properties. Each coordinate value on the frequency spectrum depends on all the image pixels in the spatial domain, representing a specific spatial frequency. Explicitly minimizing the distance of coordinate values on the real and fake spectra can help networks easily locate difficult regions on the spectrum, *i.e.*, hard frequencies.

To tackle these hard frequencies, inspired by hard example mining [9, 51] and focal loss [34], we propose a simple yet effective frequency-level objective function, named *focal frequency loss*. We map each spectrum coordinate value to a Euclidean vector in a two-dimensional space, with both the amplitude and phase information of the spatial frequency put under consideration. The proposed loss function is defined by the scaled Euclidean distance of these vectors by down-weighting easy frequencies using a dynamic spectrum weight matrix. Intuitively, the matrix is updated on the fly according to a non-uniform distribution on the current loss of each frequency during training. The model will then rapidly focus on hard frequencies and progressively refine the generated frequencies to improve image quality.

The contributions of this work are summarized as follows. 1) We propose a novel focal frequency loss, which

directly optimizes generative models in the frequency domain. The loss is complementary to existing spatial losses, offering great impedance against the loss of hard frequencies due to the inherent crux of neural networks. 2) We conduct systematic experiments demonstrating the versatility and effectiveness of the proposed loss for many common generative models [17, 31, 21, 42] to ameliorate image synthesis quality. 3) We note that the exact form of the focal frequency loss is not crucial. We provide some variants and practical considerations for the flexibility.

2. Related Work

Generative models. Recent advances [17, 31, 12, 29, 56] of generative models are built on deep neural networks, showing impressive capability in capturing high-level latent representations of images and synthesizing new data. Two popular categories of generative models are autoencoders (AE) [17, 31] and generative adversarial networks (GAN) [12]. The vanilla AE [17] reconstructs images, aiming at learning latent codes in an unsupervised manner, typically for dimensional reduction and feature learning. Autoencoders have been widely used to generate images since the development of variational autoencoders (VAE) [31, 30]. Their applications have been extended to various tasks, *e.g.*, face manipulation [2, 1, 22]. Another category of generative models is GAN [12, 39, 45], where a generator tries to fool a discriminator by refining the synthesized images constantly until the discriminator fails to perceive them as fakes. GAN is extensively applied in face generation [25, 26, 27], image-to-image translation [21, 76, 6, 23], style transfer [35, 18], and semantic image synthesis [60, 42, 36]. Existing approaches usually apply spatial domain objective functions to generate images while seldom consider improving quality via the frequency domain. Our proposed focal frequency loss presents this preliminary attempt, providing a complementary solution to ameliorate synthesis quality further on a variety of models.

Frequency domain analysis of neural networks. Recent studies have been analyzing neural networks from the frequency domain aspect. For instance, some studies [47, 38, 54] employ Fourier analysis to highlight the phenomenon of spectral bias in neural networks towards learning low-frequency functions. F-principle [68] reports that networks usually fit target functions from low to high frequencies. Using coordinate-based MLPs, Fourier features [54, 48] and positional encoding [38, 57] are adopted to recover missing high frequencies in single image regression problems. Besides, several studies have incorporated frequency analysis with network compression [13, 67, 69, 5, 14] and feature reduction [32, 61] to accelerate the training and inference of networks. The application areas of the frequency domain analysis have been further extended, including media forensics [59, 74, 19, 10], super-resolution [11, 63], generaliza-

tion analysis [58], magnetic resonance imaging [53], image rescaling [64], *etc.* Despite the wide exploration in various problems and applications, improving generative models in the frequency domain remains much less explored.

Hard example processing. Hard example processing is widely explored in object detection and image classification to address the class imbalance problem. A common solution is to use a bootstrapping technique called hard example mining [51, 9]. A representative method of hard example mining is online hard example mining (OHEM) [51], where the training examples are sampled following the current loss of each example to modify the stochastic gradient descent. The model is encouraged to learn hard examples more to boost performance. An alternative solution is focal loss [34], which is a scaled cross-entropy loss. The scaling factor dynamically down-weights the contribution of easy examples during training so that a model can focus on learning hard examples. The proposed focal frequency loss is inspired by these techniques.

3. Focal Frequency Loss

We propose a *focal frequency loss* to improve image synthesis quality of generative models by narrowing the gap between the real and fake images in the frequency domain. The loss allows the model to dynamically locate and focus on hard frequencies, *i.e.*, the frequency components that are hard to synthesize. To formulate our method, we explicitly exploit the frequency representation of images (Section 3.1), facilitating the network to locate the hard frequencies. We then define a frequency distance (Section 3.2) to quantify the differences between images in the frequency domain. Finally, we adopt a dynamic spectrum weighting scheme (Section 3.3) that allows the model to focus on the on-the-fly hard frequencies during training.

3.1. Frequency Representation of Images

In this section, we revisit and highlight several key concepts of the discrete Fourier transform and the physical meanings of different regions on the frequency spectrum. We demonstrate the effect of missing frequencies in the image and the advantage of frequency representation for locating the hard frequencies.

Discrete Fourier transform (DFT) is a complex-valued function that converts a discrete finite signal into its constituent frequencies, *i.e.*, complex exponential waves. An image² can be treated as a two-dimensional discrete finite signal with only real numbers. Thus, to convert an image into its frequency representation, we perform the 2D dis-

²For simplicity, the formulas in this section are applied to gray-scale images, while the extension to color images is straightforward by processing each channel separately in the same way.

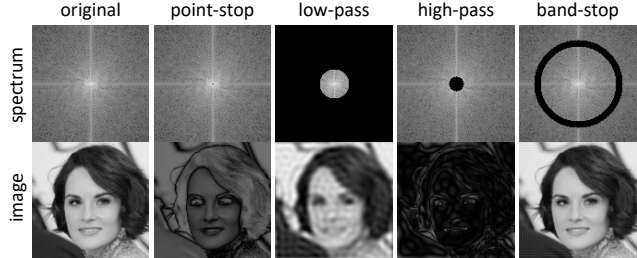


Figure 2. Standard bandlimiting operations on the frequency spectrum with the origin (low frequencies) center shifted and respective images in the spatial domain. These manual operations can be regarded as a simulation to show the effect of missing frequencies.

crete Fourier transform:

$$F(u, v) = \sum_{x=0}^{M-1} \sum_{y=0}^{N-1} f(x, y) \cdot e^{-i2\pi\left(\frac{ux}{M} + \frac{vy}{N}\right)}, \quad (1)$$

where the image size is $M \times N$; (x, y) denotes the coordinate of an image pixel in the spatial domain; $f(x, y)$ is the pixel value; (u, v) represents the coordinate of a spatial frequency on the frequency spectrum; $F(u, v)$ is the complex frequency value; e and i are Euler’s number and the imaginary unit, respectively. Following Euler’s formula:

$$e^{i\theta} = \cos \theta + i \sin \theta, \quad (2)$$

the natural exponential function in Eq. (1) can be written as:

$$e^{-i2\pi\left(\frac{ux}{M} + \frac{vy}{N}\right)} = \cos 2\pi\left(\frac{ux}{M} + \frac{vy}{N}\right) - i \sin 2\pi\left(\frac{ux}{M} + \frac{vy}{N}\right). \quad (3)$$

According to Eq. (1) and Eq. (3), the image is decomposed into orthogonal sine and cosine functions, constituting the imaginary and the real part of the frequency value, respectively, after applied 2D DFT. Each sine or cosine can be regarded as a binary function of (x, y) , where its angular frequency is decided by the spectrum position (u, v) . The mixture of these sines and cosines provides both the horizontal and vertical frequencies of an image. Therefore, spatial frequency manifests as the 2D sinusoidal components in the image. The spectrum coordinate (u, v) also represents the angled direction of a spatial frequency (visualizations can be found in the *Appendix*), and $F(u, v)$ shows the “reflection” of the image to this frequency. Due to the periodicity of trigonometric functions, the frequency representation of an image also acquires periodic properties.

Note that in Eq. (1), $F(u, v)$ is the sum of a function that traverses every image pixel in the spatial domain, hence a specific spatial frequency on the spectrum depends on all the image pixels. For an intuitive visualization, we suppress the *single* center point (the lowest frequency) of the spectrum (Column 2 of Figure 2), leading to *all* the image pixels being affected. To further ascertain the spatial frequency at the different regions on the spectrum, we perform some other standard bandlimiting operations and visualize

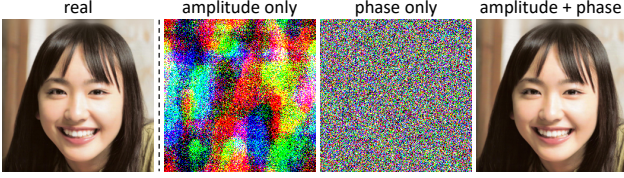


Figure 3. The necessity of both amplitude and phase information for a frequency distance verified by *single-image reconstruction*.

their physical meanings in the spatial domain (Figure 2). A low-pass filter (Column 3), *i.e.*, missing high frequencies, causes blur and typical ringing artifacts. A high-pass filter (Column 4), *i.e.*, missing low frequencies, tends to retain edges and boundaries. Interestingly, a simple band-stop filter (Column 5), *i.e.*, missing certain frequencies, produces visible checkerboard artifacts (zoom in for view), which are quite common for generative models.

Interestingly, the losses of different regions on the frequency spectrum correspond to different artifacts on the image. One may deduce that compensating for these losses may reduce artifacts and improve image generation quality. The analysis here shows the value of using the frequency representation of images for profiling and locating different frequencies, especially the hard ones.

3.2. Frequency Distance

To devise a loss function for the missing frequencies, we need a distance metric that quantifies the differences between real and fake images in the frequency domain. The distance has to be differentiable to support stochastic gradient descent. In the frequency domain, the data objects are different spatial frequencies on the frequency spectrum, appearing as different 2D sinusoidal components in an image. To design our frequency distance, we further study the real and imaginary part of the complex value $F(u, v)$ in Eq. (1).

Let $R(u, v) = a$ and $I(u, v) = b$ be the real and the imaginary part of $F(u, v)$, respectively. $F(u, v)$ can be rewritten as:

$$F(u, v) = R(u, v) + I(u, v)i = a + bi. \quad (4)$$

According to the definition of 2D discrete Fourier transform, there are two key elements in $F(u, v)$. The first element is *amplitude*, which is defined as:

$$|F(u, v)| = \sqrt{R(u, v)^2 + I(u, v)^2} = \sqrt{a^2 + b^2}. \quad (5)$$

Amplitude manifests the energy, *i.e.*, how strongly an image responds to the 2D sinusoidal wave with a specific frequency. We typically show the amplitude as an informative visualization of the frequency spectrum (*e.g.*, Figure 1 and 2). The second element is *phase*, which is written as:

$$\angle F(u, v) = \arctan\left(\frac{I(u, v)}{R(u, v)}\right) = \arctan\frac{b}{a}. \quad (6)$$

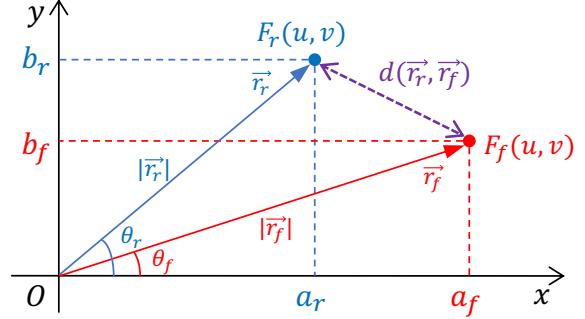


Figure 4. Frequency distance between \vec{r}_r and \vec{r}_f mapped from two corresponding real and fake frequency values $F_r(u, v)$ and $F_f(u, v)$ at the spectrum position (u, v) . The Euclidean distance (purple line) is used, considering both the amplitude (magnitude $|\vec{r}_r|$ and $|\vec{r}_f|$) and phase (angle θ_r and θ_f) information.

Phase represents the shift of a 2D sinusoidal wave from the wave with the origin value (the beginning of a cycle).

A frequency distance should consider both the amplitude and the phase as they capture different information of an image. We show a simple single-image reconstruction experiment in Figure 3. Merely minimizing the amplitude difference returns an reconstructed image with irregular color patterns. Conversely, if we only use the phase information, the synthesized image resembles a noise. A faithful reconstruction can only be achieved by considering both amplitude and phase.

Our solution is to map each frequency value to a Euclidean vector in a two-dimensional space (*i.e.*, a plane). Following the standard definition of a complex number, the real and imaginary parts correspond to the x -axis and y -axis, respectively. Let $F_r(u, v) = a_r + b_r i$ be the spatial frequency value at the spectrum coordinate (u, v) of the real image, and the corresponding $F_f(u, v) = a_f + b_f i$ with the similar meaning w.r.t. the fake image. We denote \vec{r}_r and \vec{r}_f as two respective vectors mapped from $F_r(u, v)$ and $F_f(u, v)$ (see Figure 4). Based on the definition of amplitude and phase, we note that the vector magnitude $|\vec{r}_r|$ and $|\vec{r}_f|$ correspond to the amplitude, and the angle θ_r and θ_f correspond to the phase. Thus, the frequency distance corresponds to the distance between \vec{r}_r and \vec{r}_f , which considers both the vector magnitude and angle. We simply use the (squared) Euclidean distance for a single frequency:

$$d(\vec{r}_r, \vec{r}_f) = \|\vec{r}_r - \vec{r}_f\|_2^2 = |F_r(u, v) - F_f(u, v)|^2. \quad (7)$$

The frequency distance between the real and fake images can be written as the average value:

$$d(F_r, F_f) = \frac{1}{MN} \sum_{u=0}^{M-1} \sum_{v=0}^{N-1} |F_r(u, v) - F_f(u, v)|^2. \quad (8)$$

3.3. Dynamic Spectrum Weighting

Based on the frequency distance we defined in Eq. (8), the model can quantitatively compare the real and fake im-

ages in the frequency domain instead of the spatial domain. However, a direct use of Eq. (8) as a loss function is not helpful in coping with hard frequencies since the weight of each frequency is identical. The model will still bias to easy frequencies due to the inherent crux of the networks.

Inspired by hard example mining [9, 51] and focal loss [34], our method is to focus the model training on the hard frequencies. To implement this, we further introduce a spectrum weight matrix to down-weight the easy frequencies. The spectrum weight matrix is dynamically determined by a non-uniform distribution on the current loss of each frequency during training. The shape of the matrix is the same as that of the spectrum. The matrix element $w(u, v)$, *i.e.*, the weight for the spatial frequency at (u, v) is defined as:

$$w(u, v) = |F_r(u, v) - F_f(u, v)|^\alpha, \quad (9)$$

where α is the scaling factor for the flexibility. We further normalize the matrix values into the range $[0, 1]$, where the weight 1 corresponds to the currently most lost frequency, and the easy frequencies are down-weighted. The gradient through the matrix is locked, so it only serves as the weight for each frequency.

By performing the Hadamard product for the spectrum weight matrix and the frequency distance matrix, we have the full form of the focal frequency loss:

$$\text{FFL} = \frac{1}{MN} \sum_{u=0}^{M-1} \sum_{v=0}^{N-1} w(u, v) |F_r(u, v) - F_f(u, v)|^2. \quad (10)$$

The focal frequency loss can be seen as a weighted average of the frequency distance between the real and fake images. It focuses the model on synthesizing hard frequencies by down-weighting easy frequencies using the introduced spectrum weight matrix. Besides, the focused region is updated on the fly to complement the immediate hard frequencies, thus progressively refining the generated images.

In practice, to apply the proposed focal frequency loss to a generative model, we first transform both the real and fake images into their frequency presentations using the 2D DFT. We then perform the orthonormalization for each frequency value $F(u, v)$, *i.e.*, dividing it by \sqrt{MN} , so that the 2D DFT is unitary to ensure a smooth gradient. Finally, we employ Eq. (10) to calculate the focal frequency loss.

Similar to [34], we also note that the exact form of the focal frequency loss is not crucial. There are several variants that can be considered for the flexibility. Some simple variants can be derived by adjusting the spectrum weight matrix parameter α in Eq. (9). The parameter α controls how close the values of the weight matrix are, *i.e.*, how focused the model is. In our experiments, we set $\alpha = 1$. Besides, one can attempt patch-based focal frequency loss by cropping an image into small patches so that the focused frequencies are at the patch level. Some studies on these variants are provided in the *Appendix*.

4. Experiments

4.1. Settings

Baselines. Our experiments cover different generative models in diverse tasks. We start from the image reconstruction task by vanilla AE [17] (*i.e.*, a simple 2-layer MLP) to evaluate the ability of the focal frequency loss (FFL) to help pixel-level losses maintain the original image information. We then vary the network structure to the convolutional network using VAE [31] for image reconstruction. Adopting VAE, we also extend the task to unconditional image synthesis, *i.e.*, generating images from the Gaussian noise. Besides, we visit the conditional image synthesis, *i.e.*, generating images based on certain conditions, using GAN-based methods. Specifically, we choose the image-to-image translation task. We select two typical approaches for image-to-image translation, *i.e.*, pix2pix [21] and SPADE [42]. These baselines vary in categories, network structures, tasks, and spatial losses, to verify the effectiveness and versatility of FFL for various settings. The implementation details can be found in our *Appendix*.

Datasets. We conduct experiments on a total of seven datasets under diverse settings. The datasets vary in types, sizes, and resolutions. For vanilla AE, we use the Describable Textures Dataset (DTD) [7], containing texture images with special frequency patterns. Besides, we use the cropped and aligned faces in CelebA [37], which are more natural images. For VAE, we exploit the cropped and aligned face images in CelebA and CelebA-HQ [25]. We preprocess the face images into different resolutions. For pix2pix, we utilize the officially prepared CMP Facades [46] and edges \rightarrow shoes [70] datasets. The edge maps are detected by HED [66]. For SPADE, we select two challenging datasets, *i.e.*, Cityscapes [8] and ADE20K [75]. Please refer to the *Appendix* for the dataset details.

Evaluation metrics. To quantify frequency domain difference, we introduce a frequency-level metric, named Log Frequency Distance (LFD), which is defined by a modified version of Eq. (8):

$$\text{LFD} = \log \left[\frac{1}{MN} \left(\sum_{u=0}^{M-1} \sum_{v=0}^{N-1} |F_r(u, v) - F_f(u, v)|^2 \right) + 1 \right], \quad (11)$$

where the logarithm is only used to scale the value into a reasonable range. A lower LFD is better. Note that LFD is a full reference metric, *i.e.*, requiring the ground truth (GT) image, so we use it in the reconstruction tasks.

Besides, we integrate the evaluation protocols from prior works [38, 3, 42, 23]. Specifically, we employ FID (lower is better) [16] for all tasks. For the reconstruction tasks of vanilla AE and VAE, we use PSNR (higher is better), SSIM (higher is better) [62], and LPIPS (lower is better) [73] in addition to LFD and FID. For the generation tasks of VAE and pix2pix, we apply IS (higher is better) [50] in addition

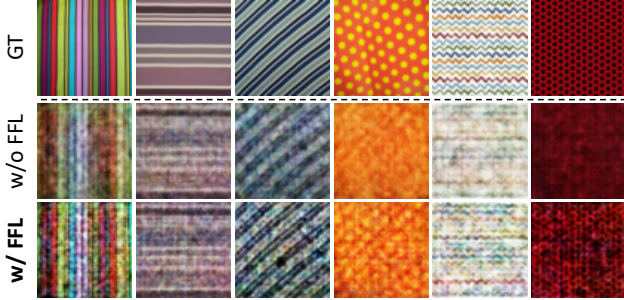


Figure 5. **Vanilla AE image reconstruction** results on the **DTD** (64×64) dataset.

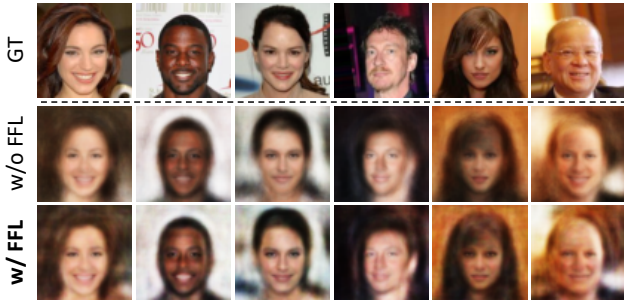


Figure 6. **Vanilla AE image reconstruction** results on the **CelebA** (64×64) dataset.

Table 1. The PSNR (higher is better), SSIM (higher is better), LPIPS (lower is better), FID (lower is better) and LFD (lower is better) scores for the **vanilla AE image reconstruction** trained with/without the focal frequency loss (FFL).

Dataset	FFL	PSNR \uparrow	SSIM \uparrow	LPIPS \downarrow	FID \downarrow	LFD \downarrow
DTD	w/o	20.133	0.407	0.414	246.870	14.764
	w/	20.151	0.400	0.404	240.373	14.760
CelebA	w/o	20.044	0.568	0.237	97.035	14.785
	w/	21.703	0.642	0.199	83.801	14.403

to FID. For SPADE (task-specific method for semantic image synthesis), besides FID, we follow their paper [42] to use mIoU and pixel accuracy (accu) for the segmentation performance of the generated images. We use DRN-D-105 [71] for Cityscapes and UperNet101 [65] for ADE20K.

4.2. Results and Analysis

Vanilla AE. The results of vanilla AE [17] image reconstruction on DTD are shown in Figure 5. Without the focal frequency loss (FFL) (Row 2), the vanilla AE baseline tends to synthesize blurry images, which lack sufficient texture details and only contain some low-frequency information. With FFL (Row 3), the reconstructed images become clearer and show more texture details. The results on CelebA are shown in Figure 6. FFL improves a series of quality problems, *e.g.*, face blur (Column 1, 2, 5), identity shift (Column 4 and 6), and expression loss (Column 3).

The quantitative evaluation results are presented in Table 1. Adding the proposed FFL to the vanilla AE baseline leads to a performance boost in most cases on the DTD and CelebA datasets w.r.t. five evaluation metrics. We note that

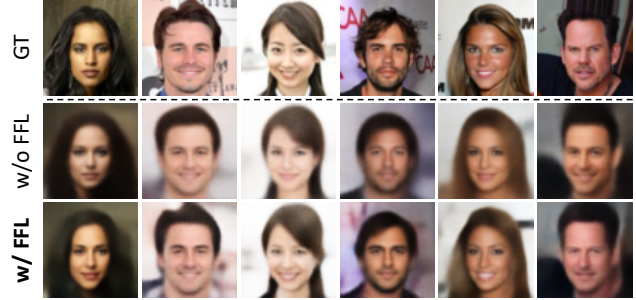


Figure 7. **VAE image reconstruction** results on the **CelebA** (64×64) dataset.

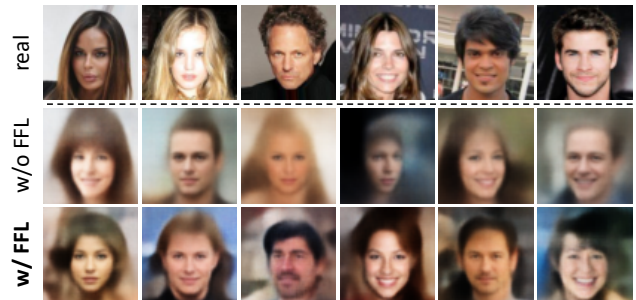


Figure 8. **VAE unconditional image synthesis** results on the **CelebA** (64×64) dataset.

Table 2. The PSNR (higher is better), SSIM (higher is better), LPIPS (lower is better), FID (lower is better) and LFD (lower is better) scores for the **VAE image reconstruction** trained with/without the focal frequency loss (FFL).

Dataset	FFL	PSNR \uparrow	SSIM \uparrow	LPIPS \downarrow	FID \downarrow	LFD \downarrow
CelebA	w/o	19.961	0.606	0.217	69.900	14.804
	w/	22.954	0.723	0.143	49.689	14.115
CelebA-HQ	w/o	21.310	0.616	0.367	71.081	17.266
	w/	22.253	0.637	0.344	59.470	17.049

the performance boost on CelebA is larger, indicating the effectiveness of FFL for the natural images.

VAE. The results of VAE [31] image reconstruction on CelebA are shown in Figure 7. FFL helps the VAE model better retain the image clarity (Column 2 and 4), expression (Column 3 and 5), and skin color (Column 1 and 6). The unconditional image synthesis results on CelebA (Figure 8) show that the quality of generated images is improved after applying FFL. The generated faces become clearer and achieve more texture details. For a higher resolution, we present the VAE image reconstruction results on CelebA-HQ in Figure 9. By adding FFL to the VAE baseline, the reconstructed images keep more original image information, *e.g.*, skin color (Column 2), mouth color (Column 1 and 4) and opening angle (Column 3). Besides, high-frequency details on the hair are clearly enhanced (Column 3). For unconditional image synthesis on CelebA-HQ (Figure 10), FFL helps reduce artifacts and ameliorates the perceptual quality of the synthesized images.

The quantitative test results of VAE image reconstruction are shown in Table 2. Adding FFL to the VAE base-



Figure 9. VAE image reconstruction results on the CelebA-HQ (256×256) dataset.



Figure 10. VAE unconditional image synthesis results on the CelebA-HQ (256×256) dataset.

Table 3. The FID (lower is better) and IS (higher is better) scores for the VAE unconditional image synthesis trained with/without the focal frequency loss (FFL).

Dataset	FFL	FID↓	IS↑
CelebA	w/o	80.116	1.873
	w/	71.050	2.010
CelebA-HQ	w/o	93.778	2.057
	w/	84.472	2.060

line achieves better performance w.r.t. all the metrics. Besides, both FID and IS are better in the unconditional image synthesis task (Table 3), which indicates that the generated images are clearer and more photorealistic. The results suggest the effectiveness of the focal frequency loss in helping VAE to improve the image generation quality.

Pix2pix. The results of pix2pix [21] image-to-image translation are shown in Figure 11. On CMP Facades, FFL improves image generation quality of pix2pix by reducing unnatural colors (Column 1) or the black artifacts on the building (Column 2). Meanwhile, the semantic information alignment with the mask becomes better after applying FFL. For the edges \rightarrow shoes translation, pix2pix baseline sometimes introduces colored checkerboard artifacts to the

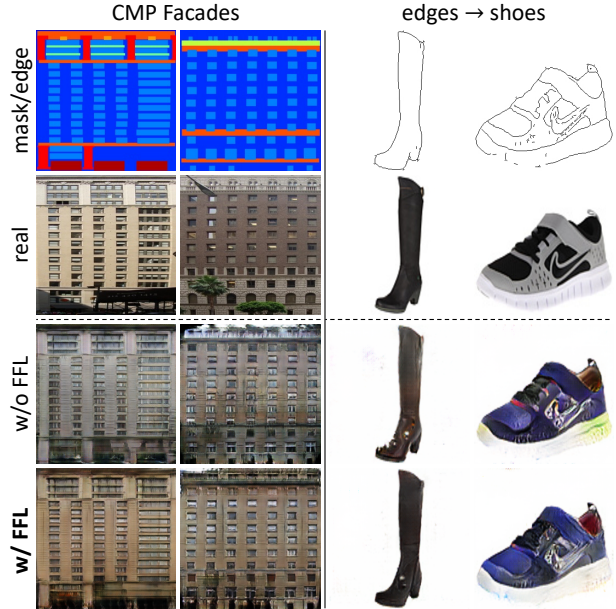


Figure 11. Pix2pix image-to-image translation results on CMP Facades (256×256) and edges \rightarrow shoes (256×256) datasets.

Table 4. The FID (lower is better) and IS (higher is better) scores for the pix2pix image-to-image translation trained with/without the focal frequency loss (FFL).

Dataset	FFL	FID↓	IS↑
CMP Facades	w/o	128.492	1.571
	w/	123.773	1.738
edges \rightarrow shoes	w/o	80.279	2.674
	w/	74.359	2.804

white background (Column 3, zoom in for view). Besides, atypical colors appear in certain cases (Column 4). In comparison, the model trained with FFL yields fewer artifacts.

The quantitative evaluation results of pix2pix image-to-image translation are shown in Table 4. FFL contributes to a performance boost on both of the two datasets. The results of the pix2pix baseline show the adaptability of the focal frequency loss for the image-to-image translation problem.

SPADE. We explore semantic image synthesis (*i.e.*, synthesizing a photorealistic image from a semantic segmentation mask) further on more challenging datasets. The results of SPADE [42] are shown in Figure 12. In the street scene of Cityscapes (Column 1), SPADE baseline distorts the car and road, missing some important details (*e.g.*, road line). The model trained with FFL demonstrates better perceptual quality for these details. In the outdoor scene of ADE20K (Column 2), applying FFL to SPADE boosts its ability to generate details on the buildings. Besides, for the ADE20K indoor images (Column 3), SPADE baseline produces some abnormal artifacts in certain cases. The model trained with the proposed FFL synthesizes more photorealistic images.

The quantitative test results are presented in Table 5 (the values used for comparison are taken from [42]). We compare SPADE trained with/without FFL against a series of



Figure 12. SPADE semantic image synthesis results on the Cityscapes (512×256) and ADE20K (256×256) datasets.

Table 5. The mIoU (higher is better), pixel accuracy (accu, higher is better) and FID (lower is better) scores for the SPADE semantic image synthesis trained with/without the focal frequency loss (FFL) compared to a series of task-specific methods.

Method	Cityscapes			ADE20K		
	mIoU \uparrow	accu \uparrow	FID \downarrow	mIoU \uparrow	accu \uparrow	FID \downarrow
CRN [4]	52.4	77.1	104.7	22.4	68.8	73.3
SIMS [44]	47.2	75.5	49.7	N/A	N/A	N/A
pix2pixHD [60]	58.3	81.4	95.0	20.3	69.2	81.8
SPADE [42]	62.3	81.9	71.8	38.5	79.9	33.9
SPADE + FFL	64.2	82.5	59.5	42.9	82.4	33.7

open-source task-specific semantic image synthesis methods [4, 44, 60]. SIMS [44] obtains the best FID but poor segmentation scores on Cityscapes in that it directly stitches the training image patches from a memory bank while not keeping the exactly consistent positions. Without modifying the SPADE network structure, training with FFL contributes a further performance boost, greatly outperforming the benchmark methods, which suggests the versatility of the focal frequency loss for diverse generative models.

Ablation studies. We present ablation studies of each key component for the focal frequency loss (FFL) in Figure 13 and the corresponding quantitative results in Table 6. For intuitiveness and simplicity, we revisit the vanilla AE image reconstruction task on CelebA.

Trained with the full FFL, the model achieves better performance than the baseline without FFL. If we do not use the frequency representation of images (Section 3.1) and dynamically focus the model on hard pixels in the spatial domain, the synthesized images will become even more blurry than the baseline. The quantitative results degrade. Discarding either the phase or amplitude information (Section 3.2) will greatly harm the metric performance. Visu-

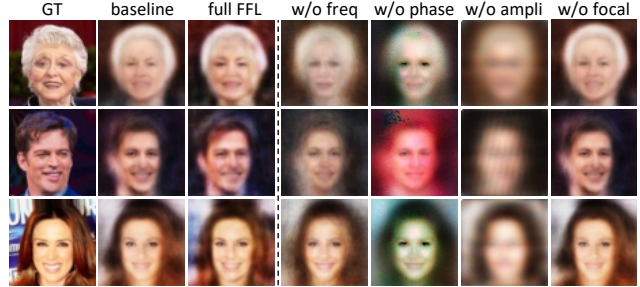


Figure 13. Ablation studies of each key component for the focal frequency loss (FFL), *i.e.*, frequency representation (freq), phase and amplitude (ampli) information, and dynamic spectrum weighting (focal) in the vanilla AE image reconstruction task on CelebA.

Table 6. The PSNR (higher is better), SSIM (higher is better), LPIPS (lower is better), FID (lower is better) and LFD (lower is better) scores for the ablation studies of each key component for the focal frequency loss (FFL).

	PSNR \uparrow	SSIM \uparrow	LPIPS \downarrow	FID \downarrow	LFD \downarrow
baseline	20.044	0.568	0.237	97.035	14.785
full FFL	21.703	0.642	0.199	83.801	14.403
w/o freq	18.200	0.470	0.265	123.833	15.210
w/o phase	13.273	0.380	0.407	233.170	16.344
w/o ampli	15.640	0.359	0.539	323.528	15.799
w/o focal	20.163	0.574	0.234	94.497	14.758

ally, using no phase information (amplitude only), the contour of the reconstructed faces will be retained, but the color is completely shifted. Without amplitude (phase only), the model cannot reconstruct the faces at all, and the full identity information is lost. This further verifies the necessity of considering both amplitude and phase information. Without focusing the model on the hard frequencies by the dynamic spectrum weighting scheme (*i.e.*, directly using Eq. (8)), the results will be visually similar to the baseline, in line with our discussion in Section 3.3. The metrics will decrease, being close to but slightly better than baseline, which may benefit from the frequency representation.

5. Discussion

We present a preliminary exploration of optimizing generative models in the frequency domain. Specifically, we propose the focal frequency loss, a generic loss function that is complementary to existing spatial losses of diverse baselines varying in categories, network structures, and tasks. Despite the succinct design, the loss dynamically focuses the model on the hard frequencies as the training proceeds, offering great impedance against the loss of crucial frequency information and ameliorating the synthesis quality.

Several topics can be interesting future works for further improvement. Incorporating unconditional GAN, which directly models a data distribution, is one direction. The solutions may include some frequency distribution comparison schemes, *e.g.*, frequency discriminator. Besides, we may further extend the focal frequency loss application areas to various low-level vision tasks such as super-resolution.

References

- [1] DeepFaceLab. <https://github.com/iperov/DeepFaceLab/>. Accessed: 2019-08-20. **2**
- [2] DeepFakes. <https://github.com/deepfakes/faceswap/>. Accessed: 2019-08-16. **2**
- [3] Andrew Brock, Jeff Donahue, and Karen Simonyan. Large scale GAN training for high fidelity natural image synthesis. In *ICLR*, 2018. **5**
- [4] Qifeng Chen and Vladlen Koltun. Photographic image synthesis with cascaded refinement networks. In *ICCV*, 2017. **8**
- [5] Wenlin Chen, James Wilson, Stephen Tyree, Kilian Q Weinberger, and Yixin Chen. Compressing convolutional neural networks in the frequency domain. In *KDD*, 2016. **2**
- [6] Yunjey Choi, Minje Choi, Munyoung Kim, Jung-Woo Ha, Sunghun Kim, and Jaegul Choo. StarGAN: Unified generative adversarial networks for multi-domain image-to-image translation. In *CVPR*, 2018. **2**
- [7] M. Cimpoi, S. Maji, I. Kokkinos, S. Mohamed, , and A. Vedaldi. Describing textures in the wild. In *CVPR*, 2014. **5, 12, 13**
- [8] Marius Cordts, Mohamed Omran, Sebastian Ramos, Timo Rehfeld, Markus Enzweiler, Rodrigo Benenson, Uwe Franke, Stefan Roth, and Bernt Schiele. The Cityscapes dataset for semantic urban scene understanding. In *CVPR*, 2016. **5, 13**
- [9] Pedro F Felzenszwalb, Ross B Girshick, David McAllester, and Deva Ramanan. Object detection with discriminatively trained part-based models. *TPAMI*, 32:1627–1645, 2009. **2, 3, 5**
- [10] Joel Frank, Thorsten Eisenhofer, Lea Schönherr, Asja Fischer, Dorothea Kolossa, and Thorsten Holz. Leveraging frequency analysis for deep fake image recognition. In *ICML*, 2020. **2**
- [11] Manuel Fritsche, Shuhang Gu, and Radu Timofte. Frequency separation for real-world super-resolution. In *ICCVW*, 2019. **2**
- [12] Ian Goodfellow, Jean Pouget-Abadie, Mehdi Mirza, Bing Xu, David Warde-Farley, Sherjil Ozair, Aaron Courville, and Yoshua Bengio. Generative adversarial nets. In *NeurIPS*, 2014. **1, 2, 12**
- [13] Lionel Gueguen, Alex Sergeev, Ben Kadlec, Rosanne Liu, and Jason Yosinski. Faster neural networks straight from JPEG. In *NeurIPS*, 2018. **2**
- [14] Seungwook Han, Akash Srivastava, Cole Hurwitz, Prasanna Sattigeri, and David D Cox. not-so-bigan: Generating high-fidelity images on a small compute budget. *arXiv preprint*, arXiv:2009.04433, 2020. **2**
- [15] Kaiming He, Xiangyu Zhang, Shaoqing Ren, and Jian Sun. Deep residual learning for image recognition. In *CVPR*, 2016. **13**
- [16] Martin Heusel, Hubert Ramsauer, Thomas Unterthiner, Bernhard Nessler, and Sepp Hochreiter. GANs trained by a two time-scale update rule converge to a local nash equilibrium. In *NeurIPS*, 2017. **5, 13**
- [17] Geoffrey E Hinton and Ruslan R Salakhutdinov. Reducing the dimensionality of data with neural networks. *Science*, 313:504–507, 2006. **1, 2, 5, 6, 12**
- [18] Xun Huang, Ming-Yu Liu, Serge Belongie, and Jan Kautz. Multimodal unsupervised image-to-image translation. In *ECCV*, 2018. **2**
- [19] Yihao Huang, Felix Juefei-Xu, Qing Guo, Xiaofei Xie, Lei Ma, Weikai Miao, Yang Liu, and Geguang Pu. FakeRetouch: Evading deepfakes detection via the guidance of deliberate noise. *arXiv preprint*, arXiv:2009.09213, 2020. **1, 2**
- [20] Sergey Ioffe and Christian Szegedy. Batch normalization: Accelerating deep network training by reducing internal covariate shift. In *ICML*, 2015. **12**
- [21] Phillip Isola, Jun-Yan Zhu, Tinghui Zhou, and Alexei A Efros. Image-to-image translation with conditional adversarial networks. In *CVPR*, 2017. **1, 2, 5, 7, 13**
- [22] Liming Jiang, Ren Li, Wayne Wu, Chen Qian, and Chen Change Loy. DeeperForensics-1.0: A large-scale dataset for real-world face forgery detection. In *CVPR*, 2020. **2**
- [23] Liming Jiang, Changxu Zhang, Mingyang Huang, Chunxiao Liu, Jianping Shi, and Chen Change Loy. TSIT: A simple and versatile framework for image-to-image translation. In *ECCV*, 2020. **1, 2, 5**
- [24] Justin Johnson, Alexandre Alahi, and Li Fei-Fei. Perceptual losses for real-time style transfer and super-resolution. In *ECCV*, 2016. **12, 13**
- [25] Tero Karras, Timo Aila, Samuli Laine, and Jaakko Lehtinen. Progressive growing of GANs for improved quality, stability, and variation. *arXiv preprint*, arXiv:1710.10196, 2017. **2, 5, 12, 13**
- [26] Tero Karras, Samuli Laine, and Timo Aila. A style-based generator architecture for generative adversarial networks. In *CVPR*, 2019. **2**
- [27] Tero Karras, Samuli Laine, Miika Aittala, Janne Hellsten, Jaakko Lehtinen, and Timo Aila. Analyzing and improving the image quality of StyleGAN. In *CVPR*, 2020. **1, 2**
- [28] Diederik P Kingma and Jimmy Ba. Adam: A method for stochastic optimization. *arXiv preprint*, arXiv:1412.6980, 2014. **12, 13**
- [29] Durk P Kingma and Prafulla Dhariwal. Glow: Generative flow with invertible 1x1 convolutions. In *NeurIPS*, 2018. **1, 2**
- [30] Durk P Kingma, Shakir Mohamed, Danilo Jimenez Rezende, and Max Welling. Semi-supervised learning with deep generative models. In *NeurIPS*, 2014. **2**
- [31] Diederik P Kingma and Max Welling. Auto-encoding variational bayes. *arXiv preprint*, arXiv:1312.6114, 2013. **1, 2, 5, 6, 12**
- [32] A Levinskas. Convolutional neural network feature reduction using wavelet transform. *Elektronika ir Elektrotechnika*, 19:61–64, 2013. **2**
- [33] Jae Hyun Lim and Jong Chul Ye. Geometric GAN. *arXiv preprint*, arXiv:1705.02894, 2017. **13**
- [34] Tsung-Yi Lin, Priya Goyal, Ross Girshick, Kaiming He, and Piotr Dollár. Focal loss for dense object detection. In *ICCV*, 2017. **2, 3, 5**

- [35] Ming-Yu Liu, Thomas Breuel, and Jan Kautz. Unsupervised image-to-image translation networks. In *NeurIPS*, 2017. [2](#)
- [36] Xihui Liu, Guojun Yin, Jing Shao, Xiaogang Wang, and Hongsheng Li. Learning to predict layout-to-image conditional convolutions for semantic image synthesis. In *NeurIPS*, 2019. [2](#)
- [37] Ziwei Liu, Ping Luo, Xiaogang Wang, and Xiaoou Tang. Deep learning face attributes in the wild. In *ICCV*, 2015. [5](#), [12](#), [13](#), [14](#)
- [38] Ben Mildenhall, Pratul P. Srinivasan, Matthew Tancik, Jonathan T. Barron, Ravi Ramamoorthi, and Ren Ng. NeRF: Representing scenes as neural radiance fields for view synthesis. In *ECCV*, 2020. [1](#), [2](#), [5](#)
- [39] Mehdi Mirza and Simon Osindero. Conditional generative adversarial nets. *arXiv preprint*, arXiv:1411.1784, 2014. [2](#), [13](#)
- [40] Takeru Miyato, Toshiki Kataoka, Masanori Koyama, and Yuichi Yoshida. Spectral normalization for generative adversarial networks. *arXiv preprint*, arXiv:1802.05957, 2018. [13](#)
- [41] Augustus Odena, Vincent Dumoulin, and Chris Olah. Deconvolution and checkerboard artifacts. *Distill*, 1:e3, 2016. [1](#)
- [42] Taesung Park, Ming-Yu Liu, Ting-Chun Wang, and Jun-Yan Zhu. Semantic image synthesis with spatially-adaptive normalization. In *CVPR*, 2019. [1](#), [2](#), [5](#), [6](#), [7](#), [8](#), [13](#)
- [43] Stanislav Pidhorskyi, Donald A Adjeroh, and Gianfranco Doretto. Adversarial latent autoencoders. In *CVPR*, 2020. [1](#)
- [44] Xiaojuan Qi, Qifeng Chen, Jiaya Jia, and Vladlen Koltun. Semi-parametric image synthesis. In *CVPR*, 2018. [8](#)
- [45] Alec Radford, Luke Metz, and Soumith Chintala. Unsupervised representation learning with deep convolutional generative adversarial networks. *arXiv preprint*, arXiv:1511.06434, 2015. [2](#)
- [46] Radim Šára Radim Tyleček. Spatial pattern templates for recognition of objects with regular structure. In *GCPR*, 2013. [5](#), [13](#)
- [47] Nasim Rahaman, Aristide Baratin, Devansh Arpit, Felix Draxler, Min Lin, Fred Hamprecht, Yoshua Bengio, and Aaron Courville. On the spectral bias of neural networks. In *ICML*, 2019. [1](#), [2](#)
- [48] Ali Rahimi and Benjamin Recht. Random features for large-scale kernel machines. In *NeurIPS*, 2008. [2](#)
- [49] Olaf Ronneberger, Philipp Fischer, and Thomas Brox. U-Net: Convolutional networks for biomedical image segmentation. In *MICCAI*, 2015. [13](#)
- [50] Tim Salimans, Ian Goodfellow, Wojciech Zaremba, Vicki Cheung, Alec Radford, and Xi Chen. Improved techniques for training GANs. In *NeurIPS*, 2016. [5](#)
- [51] Abhinav Shrivastava, Abhinav Gupta, and Ross Girshick. Training region-based object detectors with online hard example mining. In *CVPR*, 2016. [2](#), [3](#), [5](#)
- [52] Karen Simonyan and Andrew Zisserman. Very deep convolutional networks for large-scale image recognition. *arXiv preprint*, arXiv:1409.1556, 2014. [13](#)
- [53] Nalini M Singh, Juan Eugenio Iglesias, Elfar Adalsteinsson, Adrian V Dalca, and Polina Golland. Joint frequency-and image-space learning for fourier imaging. *arXiv preprint*, arXiv:2007.01441, 2020. [3](#)
- [54] Matthew Tancik, Pratul P Srinivasan, Ben Mildenhall, Sara Fridovich-Keil, Nithin Raghavan, Utkarsh Singhal, Ravi Ramamoorthi, Jonathan T Barron, and Ren Ng. Fourier features let networks learn high frequency functions in low dimensional domains. In *NeurIPS*, 2020. [1](#), [2](#)
- [55] Dmitry Ulyanov, Andrea Vedaldi, and Victor Lempitsky. Instance normalization: The missing ingredient for fast stylization. *arXiv preprint*, arXiv:1607.08022, 2016. [13](#)
- [56] Aaron Van den Oord, Nal Kalchbrenner, Lasse Espeholt, Oriol Vinyals, Alex Graves, et al. Conditional image generation with PixelCNN decoders. In *NeurIPS*, 2016. [1](#), [2](#)
- [57] Ashish Vaswani, Noam Shazeer, Niki Parmar, Jakob Uszkoreit, Llion Jones, Aidan N Gomez, Łukasz Kaiser, and Illia Polosukhin. Attention is all you need. In *NeurIPS*, 2017. [2](#)
- [58] Haohan Wang, Xindi Wu, Zeyi Huang, and Eric P Xing. High-frequency component helps explain the generalization of convolutional neural networks. In *CVPR*, 2020. [3](#)
- [59] Sheng-Yu Wang, Oliver Wang, Richard Zhang, Andrew Owens, and Alexei A Efros. CNN-generated images are surprisingly easy to spot...for now. In *CVPR*, 2020. [1](#), [2](#)
- [60] Ting-Chun Wang, Ming-Yu Liu, Jun-Yan Zhu, Andrew Tao, Jan Kautz, and Bryan Catanzaro. High-resolution image synthesis and semantic manipulation with conditional GANs. In *CVPR*, 2018. [2](#), [8](#), [13](#)
- [61] Yunhe Wang, Chang Xu, Shan You, Dacheng Tao, and Chao Xu. CNNpack: Packing convolutional neural networks in the frequency domain. In *NeurIPS*, 2016. [2](#)
- [62] Zhou Wang, Alan C Bovik, Hamid R Sheikh, and Eero P Simoncelli. Image quality assessment: from error visibility to structural similarity. *TIP*, 13:600–612, 2004. [5](#)
- [63] Yunxuan Wei, Shuhang Gu, Yawei Li, and Longcun Jin. Unsupervised real-world image super resolution via domain-distance aware training. *arXiv preprint*, arXiv:2004.01178, 2020. [2](#)
- [64] Mingqing Xiao, Shuxin Zheng, Chang Liu, Yaolong Wang, Di He, Guolin Ke, Jiang Bian, Zhouchen Lin, and Tie-Yan Liu. Invertible image rescaling. In *ECCV*, 2020. [3](#)
- [65] Tete Xiao, Yingcheng Liu, Bolei Zhou, Yuning Jiang, and Jian Sun. Unified perceptual parsing for scene understanding. In *ECCV*, 2018. [6](#)
- [66] Saining Xie and Zhuowen Tu. Holistically-nested edge detection. In *ICCV*, 2015. [5](#), [13](#)
- [67] Kai Xu, Minghai Qin, Fei Sun, Yuhao Wang, Yen-Kuang Chen, and Fengbo Ren. Learning in the frequency domain. In *CVPR*, 2020. [2](#)
- [68] Zhi-Qin John Xu, Yaoyu Zhang, Tao Luo, Yanyang Xiao, and Zheng Ma. Frequency principle: Fourier analysis sheds light on deep neural networks. *arXiv preprint*, arXiv:1901.06523, 2019. [2](#)
- [69] Jaejun Yoo, Youngjung Uh, Sanghyuk Chun, Byeongkyu Kang, and Jung-Woo Ha. Photorealistic style transfer via wavelet transforms. In *ICCV*, 2019. [2](#)

- [70] Aron Yu and Kristen Grauman. Fine-grained visual comparisons with local learning. In *CVPR*, 2014. 5, 13
- [71] Fisher Yu, Vladlen Koltun, and Thomas Funkhouser. Dilated residual networks. In *CVPR*, 2017. 6
- [72] Han Zhang, Ian Goodfellow, Dimitris Metaxas, and Augustus Odena. Self-attention generative adversarial networks. *arXiv preprint*, arXiv:1805.08318, 2018. 13
- [73] Richard Zhang, Phillip Isola, Alexei A Efros, Eli Shechtman, and Oliver Wang. The unreasonable effectiveness of deep features as a perceptual metric. In *CVPR*, 2018. 5
- [74] Xu Zhang, Svebor Karaman, and Shih-Fu Chang. Detecting and simulating artifacts in gan fake images. In *WIFS*, 2019. 1, 2
- [75] Bolei Zhou, Hang Zhao, Xavier Puig, Sanja Fidler, Adela Barriuso, and Antonio Torralba. Scene parsing through ADE20K dataset. In *CVPR*, 2017. 5, 13
- [76] Jun-Yan Zhu, Taesung Park, Phillip Isola, and Alexei A Efros. Unpaired image-to-image translation using cycle-consistent adversarial networks. In *ICCV*, 2017. 2

Appendix

This appendix provides supplementary information that is not elaborated in our main paper: Section A shows visualizations of 2D sinusoidal components with specific spatial frequencies in an image. Section B describes the implementation details of all the baselines in our experiments. Section C details our used datasets under diverse settings. Section D provides some studies on the variants of focal frequency loss. Section E presents more analysis of the results.

A. Spatial Frequency Visualization

After applying 2D discrete Fourier transform, an image is converted into its frequency representation and decomposed into orthogonal sine and cosine functions. The angular frequency of each sine and cosine function is decided by the frequency spectrum coordinate (u, v) . The spatial frequency manifests as the 2D sinusoidal components in the image. The spectrum coordinate also represents the angled direction of a specific spatial frequency. As an intuitive view, we show some examples of the 2D sinusoidal components with specific spatial frequencies in Figure 14. It is observed that the angled direction and density (angular frequency) of the waves depend on the spectrum coordinate (u, v) . Besides, the complex frequency value $F(u, v)$ can be regarded as the weight for each wave, and the weighted sum corresponds to the whole image in the spatial domain.

B. Implementation Details

The code used for our experiments will be made publicly available. In this section, we will provide the implementation details of all the baseline methods for different tasks. We select four typical methods from the two popular generative model categories: autoencoder-based and GAN-based. Besides, we evaluate different network structures. Specifically, we explore the multilayer perceptron (MLP) network and convolutional neural network (CNN). For CNN, the network details also vary, e.g., with or without the skip connections. In addition, we consider various basic spatial domain losses, e.g., MSE loss, L1 loss, GAN loss [12], perceptual loss [24], etc., to test the ability of focal frequency loss to complement these losses. All the experiments are conducted on the NVIDIA Tesla V100 GPUs with 32 GB memory capacity.

Vanilla AE. Vanilla autoencoder [17] learns the image latent representation in an unsupervised manner, traditionally used for dimension reduction and feature learning. We employ vanilla AE in the image reconstruction task. The network is a simple 2-layer MLP with a hidden size of 256. We adopt ReLU activations (except the last layer using Tanh) and no norm layers. We use Adam [28] optimizer and set $\beta_1 = 0.9, \beta_2 = 0.999$. The learning rate is 0.001. Normal

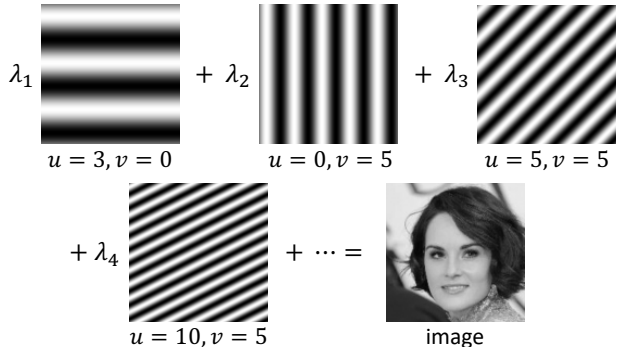


Figure 14. Two-dimensional sinusoidal components with specific spatial frequencies in an image. The angled direction and density (angular frequency) of the waves depend on the spectrum coordinate (u, v) , and $F(u, v)$ can be seen as the weight for each wave.

initialization (with mean 0.0 and standard deviation 0.02) is applied to all the networks of vanilla AE. The spatial loss is MSE loss. The models are trained on 1 GPU with a batch size of 128. We perform 200 epochs of training on DTD [7] and 20 epochs of training on CelebA [37].

VAE. Exploiting a reparameterization trick, the variational autoencoder [31] generates images by learning the latent representation in a probability distribution manner. We use VAE for image reconstruction and unconditional image synthesis. We employ CNN for VAE, with typical convolution and transposed convolution layers. Batch normalization [20] and Leaky ReLU (with the negative slope 0.2, except the last layer using Tanh) are applied. Each convolution layer has the kernel size 4×4 , stride 2, and zero-padding amount 1. In the encoder, the feature map resolution is halved after each convolution block. Images are down-sampled to 4×4 , so the number of blocks depends on the input size (e.g., if the input size is 64×64 , there will be 4 blocks). After an input layer, the number of feature channel is 64. Then, the number of feature channel will double after each convolution block, while we set a maximum channel number to 512 to avoid using redundant parameters. We apply two linear layers to the encoded feature to learn μ and σ for the reparameterization. The latent size is 256. After reparameterization, an additional linear layer is used to adjust the feature to the original shape. In the decoder, the network structure is completely inverse to the encoder by replacing convolution layers with the transposed convolution layers. We use Adam [28] optimizer and set $\beta_1 = 0.9, \beta_2 = 0.999$. The learning rate is 0.001. Normal initialization (with mean 0.0 and standard deviation 0.02) is applied to all the networks of VAE. The spatial losses are MSE loss and KL divergence loss. The models are trained on 1 GPU with a batch size of 128. We train our models for 20 epochs on CelebA [37] and 400 epochs on CelebA-HQ [25].

Pix2pix. Pix2pix [21] uses conditional GAN [39] as a general-purpose solution to image-to-image translation with training pairs. We employ pix2pix for conditional image synthesis. The U-Net [49] generator is applied, which is an encoder-decoder with skip connections between mirrored layers in the encoder and decoder stacks. There are 8 skip connection blocks in the generator. The patch-based discriminator is used. Adam [28] optimizer is used with $\beta_1 = 0.5, \beta_2 = 0.999$. The learning rate is 0.0002. Normal initialization (with mean 0.0 and standard deviation 0.02) is applied to all the networks of pix2pix. The spatial losses are vanilla GAN loss and L1 loss. The models are trained on 1 GPU. We conduct 200 epochs of training on CMP Facades [46] with a batch size of 1. We train the models for 15 epochs on edges \rightarrow shoes [70] with a batch size of 4. For other detailed network structures and parameters, we follow the original paper [21] and their released code.

SPADE. As a task-specific GAN-based method for semantic image synthesis (*i.e.*, synthesizing a photorealistic image from a semantic segmentation mask), SPADE [42] resizes the segmentation mask for modulating the activations in normalization layers by a learned affine transformation. The generator is built on a series of residual blocks [15] with the synchronized version of batch normalization. The multi-scale patch-based discriminator [60] with the instance normalization [55] is exploited. Besides, spectral normalization [40] is applied to all the convolutional layers in the generator and discriminator. Adam [28] optimizer is exploited with $\beta_1 = 0, \beta_2 = 0.9$. Two time-scale update rule [16] is applied, where the learning rates for the generator and the discriminator are 0.0001 and 0.0004, respectively. The spatial losses are hinge-based GAN loss [33, 40, 72], perceptual loss [24] calculated by VGG-19 [52] model, and feature matching loss [60]. The models are trained for 200 epochs on Cityscapes [8] and ADE20K [75] using 4 GPUs. The batch size is 32. For other detailed network structures and parameters, we follow the original paper [42] and their released code.

C. Dataset Details

In this section, we will provide detailed information about the seven datasets we explored. The datasets vary in types, sizes, and resolutions.

- **Describable Textures Dataset (DTD).** We use DTD provided by [7], which is an evolving collection of textural images in the wild, annotated with human-centric attributes. We perform vanilla AE image reconstruction using this dataset, with 4,512 images for training and 1,128 images for testing. The original images are scaled and center cropped to 64×64 .
- **CelebA.** CelebA [37] is a large-scale face attributes dataset covering large pose variations and background

clutter. We conduct image reconstruction with vanilla AE and VAE on CelebA. Besides, we perform VAE unconditional image synthesis on CelebA. We use the cropped and aligned faces. The training set contains 199,599 images, and the test set has 3,000 images. The images are resized and center cropped to 64×64 .

- **CelebA-HQ.** CelebA-HQ is a higher-quality version of the CelebA dataset provided by [25]. The original resolution is 1024×1024 . We perform VAE image reconstruction and unconditional image synthesis on this dataset. The dataset is randomly split, yielding 27,000 images for training and 3,000 images for evaluation. All the cropped and aligned face images are uniformly resized to 256×256 .
- **CMP Facades.** For pix2pix image-to-image translation, we utilize the officially prepared CMP Facades [46] dataset. The facades are collected from different cities around the world with diverse architectural styles. CMP Facades contains architectural labels and photos, which is suitable for *mask* \rightarrow *image* translation. The sizes of training and test sets are 400 and 106, respectively. The resolution is 256×256 .
- **Edges \rightarrow shoes.** We also exploit the officially prepared edges \rightarrow shoes dataset for pix2pix image-to-image translation. The shoe images are from UT Zappos50K [70]. The shoes are centered on a white background. The edge maps are detected by HED [66]. The numbers of images for training and testing are 49,825 and 200, respectively. The image size is 256×256 .
- **Cityscapes.** We use Cityscapes [8] dataset for SPADE semantic image synthesis. Cityscapes dataset consists of street scene images that are mostly collected in Germany. The dataset provides instance-wise, dense pixel annotations of 30 classes. The training set has 2,975 images, and the test set contains 500 images. The images are scaled to 512×256 .
- **ADE20K.** ADE20K [75] dataset contains challenging in-the-wild images with fine annotations of 150 semantic classes. We also use ADE20K for SPADE semantic image synthesis, with 20,210 images for training and 2,000 images for evaluation. All the images are resized to 256×256 .

D. Variant Studies

In our main paper, we mentioned that the exact form of the proposed focal frequency loss (FFL) is not crucial. We provided some variants to extend and modify FFL. In this section, we will show some studies on these variants. For

Table 7. The PSNR (higher is better), SSIM (higher is better), LPIPS (lower is better), FID (lower is better) and LFD (lower is better) scores for the **variant studies** on the spectrum weight matrix **parameter** α for the focal frequency loss.

	PSNR \uparrow	SSIM \uparrow	LPIPS \downarrow	FID \downarrow	LFD \downarrow
baseline	20.044	0.568	0.237	97.035	14.785
$\alpha = 1$ (main)	21.703	0.642	0.199	83.801	14.403
$\alpha = 2$	21.376	0.621	0.203	102.329	14.478
$\alpha = 0.5$	21.521	0.635	0.197	82.561	14.445
$\alpha = 0.1$	20.497	0.591	0.225	89.792	14.681

Table 8. The PSNR (higher is better), SSIM (higher is better), LPIPS (lower is better), FID (lower is better) and LFD (lower is better) scores for the **variant studies** on **patch-based** focal frequency loss. Patch factor p is the number of patches on each edge.

	PSNR \uparrow	SSIM \uparrow	LPIPS \downarrow	FID \downarrow	LFD \downarrow
baseline	20.044	0.568	0.237	97.035	14.785
$p = 1$ (main)	21.703	0.642	0.199	83.801	14.403
$p = 2$	21.836	0.648	0.185	88.475	14.372
$p = 4$	21.752	0.643	0.170	90.612	14.392
$p = 8$	21.414	0.627	0.176	102.334	14.470

simplicity and intuitiveness, we revisit the vanilla AE image reconstruction task on CelebA. We report quantitative evaluation results for the variant studies. The visual results of variants are similar.

Several simple variants can be derived by adjusting the spectrum weight matrix parameter α . The parameter α controls how close the weight matrix values are, *i.e.*, how focused the model is. The larger α is, the model will be more focused on the hard frequencies, *i.e.*, the weight difference for easy and hard frequencies will be larger. For the experiments we present in our main paper, we set $\alpha = 1$ (we call the main version). The results are shown in Table 7. Applying the main version of FFL ($\alpha = 1$) shows better performance than the baseline without FFL in all the five metrics. If we set $\alpha = 2$, the quantitative results degrade from the main version, especially FID. This suggests that the model may be too focused on the hard frequencies while ignoring some important easy frequency information, albeit the results are still better than the baseline in most cases. When setting $\alpha = 0.5$, all the metric results are better than the baseline. The LPIPS and FID scores become better than the main version. The results of this variant are close to the main version of FFL. If we set $\alpha = 0.1$, the quantitative results degrade from the main version despite still better than the baseline. This indicates that the model may be too unfocused. For a trade-off, we select $\alpha = 1$ as the main version of FFL, while one may consider choosing other variants regarding the parameter α in certain tasks for the flexibility.

Besides, we study another category of variants, the patch-based focal frequency loss, where we crop an image into small patches so that the focused frequencies are at the patch level. We define the patch factor p as the number of patches on each edge. For instance, if $p = 2$, the image

will be cropped into $2 \times 2 = 4$ patches. Obviously, using the original image without cropping it into patches, *i.e.*, the main version of FFL we defined before, corresponds to $p = 1$. The results are shown in Table 8. We note that $p = 1, 2, 4$ achieve close performance regarding the five evaluation metrics, all of which are much better than the baseline. However, if we set $p = 8$, the quantitative performance will degrade from the previous versions, especially FID. Although the results are still better than the baseline in most cases, this indicates that the patch size should not be too small. We simply choose $p = 1$ as the main version of FFL for our experiments in the main paper. However, the variant studies show that the patch-based focal frequency loss may contribute to an additional performance boost in certain cases. Thus, this may be another direction to extend and modify FFL.

E. More Analysis of Results

E.1. Frequency Domain Gap

As mentioned in the main paper, we wish to improve the image synthesis quality by narrowing the frequency domain gap between the real and generated images using the proposed focal frequency loss (FFL). We show some examples of VAE image reconstruction on the CelebA [37] dataset and provide more analysis about the frequency domain gap in this section.

The results are shown in Figure 15. In the spatial domain, without applying FFL, the reconstructed faces are blurry. This may be attributed to the reparameterization operation in the latent space between the encoder and decoder, which increases the difficulty for reconstruction. Trained with FFL, the VAE model can synthesize much clearer results, being closer to the ground truth images. The perceptual quality is better after applying FFL. In the frequency domain, in line with our visualizations in the main paper, the VAE baseline without FFL bias to a limited spectrum region, losing high-frequency information (outer regions and corners). The frequency domain gaps are clearly narrowed after adopting FFL. The spectrum distribution becomes closer to the ground truth. Besides, some essential special spectrum patterns can be generated by applying FFL. This suggests the effectiveness of focal frequency loss to narrow the frequency domain gaps and ameliorate image generation quality further.

E.2. Training Loss

In the main paper, we have mentioned that the proposed focal frequency loss (FFL) is complementary to existing spatial losses, *e.g.*, MSE loss, to improve the image synthesis quality. We further analyze the training loss in this section. We choose the vanilla AE image reconstruction task on CelebA [37] for simplicity. We plot the spatial losses

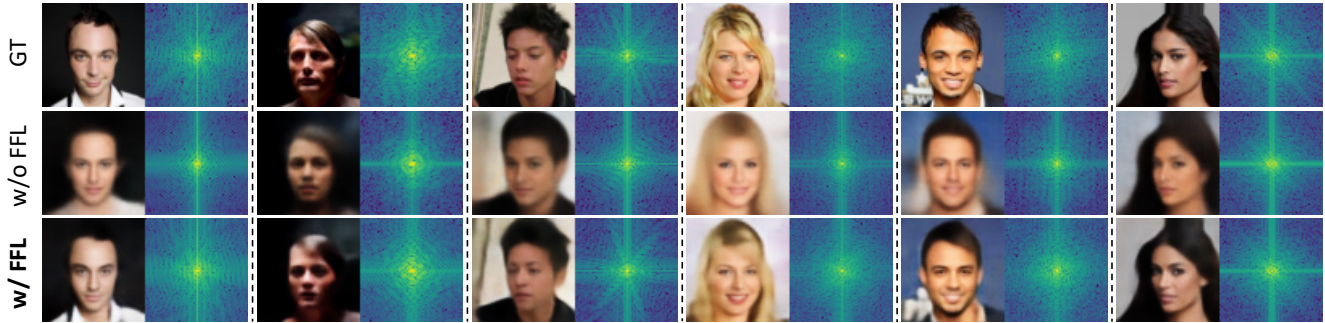


Figure 15. Frequency domain gaps are narrowed by the focal frequency loss (FFL) for VAE image reconstruction on CelebA.

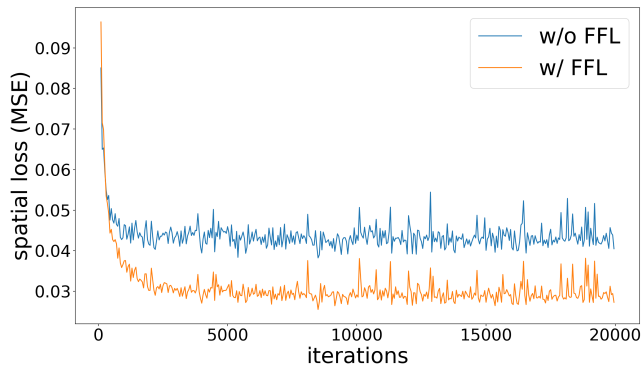


Figure 16. The spatial losses (MSE) with the same weight and random seed of the two training processes with/without focal frequency loss (FFL) for vanilla AE image reconstruction on CelebA. The spatial loss converges to a lower point with the help of FFL.

with the same weight and random seed of the two training processes with/without FFL in Figure 16. It is readily observed that the spatial loss (MSE) converges to a lower point after applying FFL. This indicates that the model may converge to a better point with the help of FFL, in line with the better perceptual quality and quantitative performance we presented in our main paper.